ARTICLE   OPEN

Check for updates

Biodegradable germanium electronics for integrated biosensing of physiological signals

Haonan Zhao[1], Zhongying Xue[2], Xiaozhong Wu[1], Zhihuan Wei[1], Qiuyu Guo[3], Miao Xu [iD][3], Chunyan Qu[4], Chunyu You[4], Yongfeng Mei [iD][4,5,6 ✉], Miao Zhang[2], Zengfeng Di[2 ✉] and Qinglei Guo [iD][1,2,5 ✉]

Transient electronics that can disappear or degrade via physical disintegration or chemical reaction over a pre-defined operational period provide essential for their applications in implantable bioelectronics due to the complete elimination of the second surgical extraction. However, the dissolution of commonly utilized bioresorbable materials often accompanies hydrogen production, which may cause potential or irreparable harm to the human body. This paper introduces germanium nanomembrane-based bioresorbable electronic sensors, where the chemical dissolution of all utilized materials in biofluidic theoretically have no gaseous products. In particular, the superior electronic transport of germanium enables the demonstrated bioresorbable electronic sensors to successfully distinguish the crosstalk of different physiological signals, such as temperature and strain, suggesting the significant prospect for the construction of dual or multi-parameter biosensors. Systematical studies reveal the gauge factor and temperature coefficient of resistance comparable to otherwise similar devices with gaseous products during their dissolution.

INTRODUCTION

Recent advances in unusual electronic materials, fabrication strategies, and device designs have built the basis for the development of bioresorbable electronic implants[1–5], which can provide diagnostic and/or therapeutic treatments for human diseases. Examples include various types of functional electronic devices, such as electrical simulators for nonpharmacological neuroregeneration[6], sensors for the monitoring of tissue or human health status[7], power supply devices for the electronic bioimplants[8,9], and many others. Such implantable electronic platforms, also known as transient electronics, offer several advantages for biomedical applications[10–12], most significantly in the elimination of the second surgical extraction because they are degradable and bioresorbable within human body over a pre-defined stable operation. Recent works have utilized inorganic or organic semiconductors as the active component of the fabricated transient electronic devices/systems[13–19]. And continuous efforts are devoted to enhance the device performance, functionalities, and reliability of these implantable transient electronics. However, the potential risks of gaseous products generated via the hydrolysis reaction of traditional transient electronics in biofluidic have not yet drawn significant attention. In particular, the aggregation of hydrogen products, which is normally found in the dissolution of element materials, may cause a toxic effect to tissue once exceeds a specific level[20–22]. Although other candidates, such as zinc oxide (ZnO)[23], indium gallium zinc oxide (IGZO)[24], and biodegradable organic semiconductors[5,25], have no gaseous products during their degradation according to their chemical reaction mechanisms, one or more disadvantages involve in moderate device performance, poor compatibility with state-of-the-art semiconductor fabrication technology, or partial degradability.

One of the most reliable approach to address the above issue involve in the reduction of dissolution rate, which accompanies slow formation speed of gaseous products[20]. With optimized modification of the active layers, slow degradation of a transient electronic implant is expectable. Previous report demonstrated that the dissolution rate of silicon could be significantly reduced by the increase of the doping concentration[26]. From the viewpoint of device functionality, however, the expanded use of a pure highly-doped silicon is limited, since most of silicon-based electronic devices involve in both high-doping and low-doping concentration regions. Therefore, important considerations in the choice of active materials for implanted transient electronics include: (i) carrier mobility for high-performance devices; (ii) compatibility with the state-of-the-art process for device fabrication; (iii) flexibility for reducing the mechanical mismatch between device and tissue/organs; (iv) biocompatibility and biodegradability after their implantation; (v) ability for reducing or eliminating the gaseous products.

Here, we demonstrate a biodegradable electronic sensor, with integrated biosensing ability of multiple physiological signals by utilizing germanium nanomembranes as the active materials. Key advantages of germanium nanomembranes are in capabilities for theoretically eliminating the gaseous products during the dissolution. Moreover, germanium has a small forbidden bandwidth and large carrier mobility, thus leading to small transit time and high operation speed[27,28], of relevance to fast signal acquisition and high-frequency device. The fabricated germanium-based sensors can distinguish the crosstalk of different physiological signals, such as temperature and strain. Systematic studies reveal that the variation in temperature has negligible effect on the gauge factor (GF) of the biodegradable germanium-based sensor, and the temperature coefficient of

[1]School of Microelectronics, Center of Nanoelectronics, Shandong University, 250100 Jinan, P. R. China. [2]State Key Laboratory of Functional Materials for Informatics, Shanghai Institute of Microsystem and Information Technology, Chinese Academy of Sciences, 200050 Shanghai, P. R. China. [3]Department of Hematology, Qilu Hospital, Cheeloo College of Medicine, Shandong University, 250100 Jinan, P. R. China. [4]Department of Materials Science, International Institute for Intelligent Nanorobots and Nanosystems, Fudan University, 200433 Shanghai, P. R. China. [5]State Key Laboratory of ASIC and Systems, Fudan University, 200433 Shanghai, P. R. China. [6]Institute of Optoelectronics, Yiwu Research Institute, Fudan University, 200433 Shanghai, P. R. China. ✉email: yfm@fudan.edu.cn; zfdi@mail.sim.ac.cn; qlguo@sdu.edu.cn
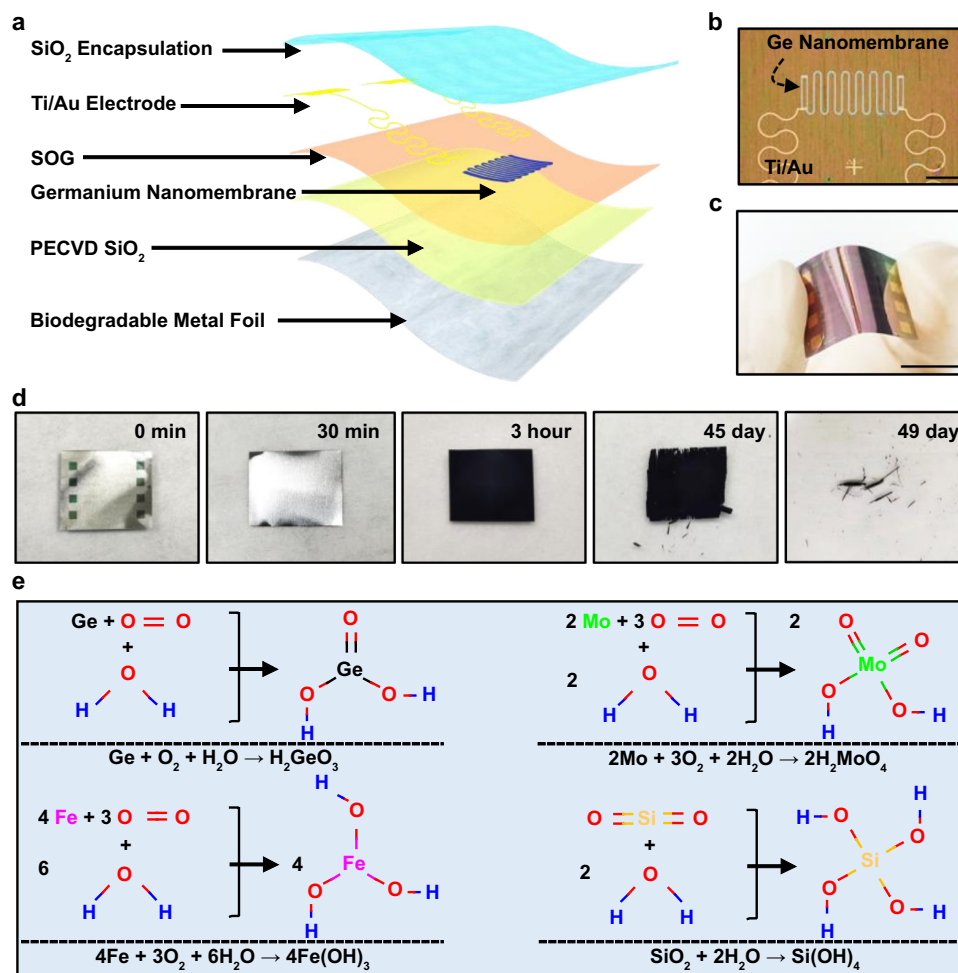
Fig. 1 Key materials and dissolution chemistries. a Exploded schematic diagram of the key components and materials of a biodegradable germanium nanomembrane-based sensor. **b** Optical microscope image of the sensor. Scale bar is 400 μm. **c** Optical image of a 2 × 2 sensor array at the bending state, suggesting good flexibility of the device. Scale bar is 1 cm. **d** Optical images of the accelerated dissolution of a biodegradable sensor in PBS (pH = 7.4, 90 °C) at different time frames. **e** Chemical equations of each of the constituent materials reacting with water, and all of the reactions theoretically have no gaseous products.

resistance (TCR) also keeps as constant at different strain levels, thus providing basis for the integrated biosensing of multiple physiological signals. These presented results demonstrate the significant potential for the use of germanium in high-performance and reliable transient electronic implants.

RESULTS AND DISCUSSION
Key materials and components of biodegradable germanium-based sensors

Figure 1a illustrates key materials and exploded schematics of the biodegradable electronic sensor. The multilayer device configuration from the bottom to the top consists of an iron (Fe) or molybdenum (Mo) foil as the flexible substrate with a thickness of approximately 30 μm, a 200 nm-thick SiO_2 layer grown by plasma-enhanced chemical vapor deposition (PECVD) as the insulator, a spin-on-glass (SOG) as the adhesive layer to facilitate the following transfer of germanium nanomembranes, a single-crystalline germanium nanomembrane with a thickness of 200 nm serving as the active layer, ultrathin gold (Au, 30 nm) nanomembrane electrodes deposited by e-beam evaporation, and a PECVD-grown SiO_2 layer (200 nm) as the encapsulation layer. The optical microscope image of a typical fabricated device appears in Fig. 1b. The sensitive germanium nanomembrane is defined into a serpentine geometry with a width of 20 μm. Previous studies have

pointed out that the critical bending radius and flexural rigidity of silicon significantly decrease with the reduction of thickness[29,30]. In this regard, the fabricated germanium nanomembrane-based sensor also exhibits good flexibility, as demonstrated in Fig. 1c. Figure 1d shows a set of images collected from a biodegradable germanium-based sensor on Mo foil at various times of immersion in phosphate buffer saline (PBS) (pH = 7.4, 90 °C). The variation in electrical resistance of the sensor at different dissolution periods is shown in Supplementary Fig. 1. Negligible variation is observed until a 12-h soaking. Complete dissolution of the device occurs after 49 days at this accelerated dissolution condition. In vitro cell culture evaluations of cytotoxicity associated with germanium nanomembranes are shown in Supplementary Fig. 2, which suggests a good biocompatibility[27]. Although Au is normally known as chemically inert, recent studies demonstrated that Au nanoparticles (4–22 nm in diameter) were nontoxic, biocompatible[31], and biodegradable in vitro by cells[32]. For in vivo applications, the implanted Au nanomaterials will stimulate an oxidative liberation of Au ions through the immune system[33]. The released Au ions if in excess will bind to sulfhydryl species to form complexes, which might be phagocytosed by mast cells and macrophages[33–36]. Small Au particles (less than 5 nm in diameter) can be directly phagocytosed by phagocytes[31]. All these investigations build bases for Au that can serve as biodegradable electrodes of implantable electronics[37].
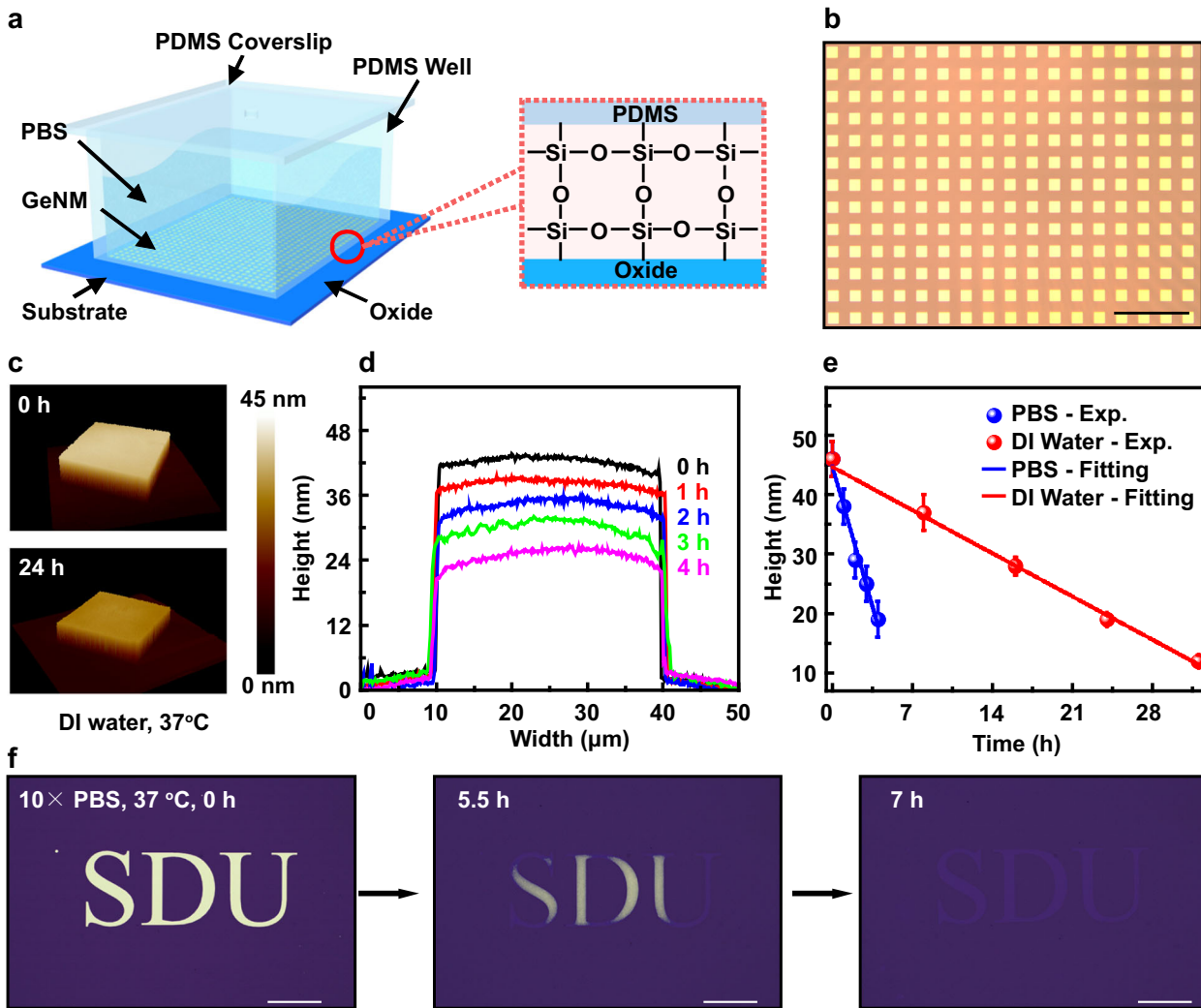
Fig. 2 **Dissolution of germanium nanomembranes. a** Schematic diagram of the key components and materials for testing the dissolution behaviors of germanium nanomembranes. The right highlights the chemical bonds between UV-ozone-treated PDMS and silicon dioxide. **b** Optical microscope image of a germanium relief array, which is formed directly on a GOI wafer. Scale bar is 200 μm. **c** AFM images of a typical germanium relief, with a dimension of $30 \times 30 \, \mu m$, at different dissolution periods (top: 0 h; bottom: 24 h) in DI water (37 °C). **d** AFM profiles of a typical germanium relief at different dissolution periods in 10× PBS (pH = 7.4, 37 °C). **e** Experimental (symbols) and fitted (lines) changes in thickness varying with dissolution time for germanium nanomembranes soaked in 10× PBS (pH = 7.4, 37 °C, blue) and DI water (37 °C, red). Error bars indicate standard deviations. **f** Optical microscope images of germanium nanomembrane-based "SDU" logo at different dissolution time frames. Scale bar is 100 μm.

The chemical reactions of other utilized biodegradable materials appear in Fig. 1e, $2Mo + 3O_2 + 2H_2O \rightarrow 2H_2MoO_4$, $4Fe + 3O_2 + 6H_2O \rightarrow 4Fe(OH)_3$, $SiO_2 + 2H_2O \rightarrow Si(OH)_4$, where no gaseous products exist, leading to improved safety and reliability of the fabricated sensor as the biomedical implants. Notably, the use of germanium nanomembrane as the active layer is important. As summarized in Supplementary Fig. 3, germanium has the highest carrier mobility compared to other biodegradable semiconductors[38], offering significant potential for the following construction of high-performance sensors or integrated sensors. The full compatibility with state-of-the-art semiconductor technology enables the convenience and large-scale production of germanium-based transient electronics. The utilized germanium nanomembrane, with a thickness of about 200 nm, also has a good flexibility[30], thus satisfying the mechanical requirement for the possible applications in bioelectronic implants. The full degradability (see the following results) of germanium builds up the fundamentals for transient electronics[27]. Besides, the dissolution of germanium in biofluidic, in a hydrolysis reaction manner,

theoretically have no gaseous products, which can eliminate the potential risks to tissue or organ induced by the accumulated gaseous products[39]. Experimental demonstrations about the non-gaseous dissolution process of germanium are shown in Supplementary Fig. 4, and the dissolution of silicon is utilized as a control.

Dissolution mechanism of germanium nanomembranes

To further understand the dissolution properties of germanium nanomembranes, square relief array with a dimension of $30 \, \mu m \times 30 \, \mu m$ and a spacing of 30 μm is fabricated on a germanium-on-insulator (GOI). Systematical studies are performed by utilizing a polydimethylsiloxane (PDMS) well as the container, which forms intimate chemical bonds with the exposed buried oxide of the patterned GOI, for bio-fluidics, as schematically shown in Fig. 2a, including deionized water (DI water) and PBS. Figure 2b shows an optical microscope image of germanium nanomembrane relief array. Figure 2c shows the atomic force microscope (AFM) images of a typical germanium nanomembrane relief at two

different dissolution periods, i.e., 0 h and 24 h, in DI water (37 °C). Similar results are also demonstrated by the scanning electron microscope (SEM) measurement, as shown in Supplementary Fig. 5. Line cuts obtained from AFM across the germanium nanomembrane relief at different dissolution periods in PBS (pH = 7.4, 37 °C) appear in Fig. 2d. A droplet-like surface of the germanium nanomembrane relief forms as the dissolution proceeds, e.g., 4 h (see the pink curve in Fig. 2d), which is attributed to the simultaneous lateral degradation effect, thus resulting in a much faster dissolution rate at the relief edge compared to the middle region. Figure 2f visually verifies this simultaneous lateral degradation effect. The defined germanium nanomembrane-based letters "SDU", with a format of Time New Roman, have a much faster dissolution rate at the position that has a much narrower lateral size, as shown in the middle panel of Fig. 2f. Nevertheless, after a 7 h immersion in PBS, the defined "SDU" is completely dissolved, as shown in the right panel of Fig. 2f. These presented results confirm a good degradability of germanium either in DI water and PBS. Figure 2e summarizes the height of germanium relief varying with the dissolution time in DI water (red dots) and PBS (blue dots), and the linear fitting infers a dissolution rate of ~6.5 nm h^{-1} in PBS (pH = 7.4, 37 °C) and ~1 nm h^{-1} in DI water (37 °C), respectively.

Since the utilized germanium nanomembrane of GOI wafer is single-crystalline, the dense atomic structure will prevent the biofluidic from entering the interior of the crystal. As a result, the thickness of germanium nanomembrane is uniformly reduced as the degradation proceeds, as demonstrated by the high-resolution transmission electron microscope (HR-TEM) measurement (see Supplementary Fig. 6). Therefore, the hydrolysis reaction of germanium nanomembrane with biofluidic has a similar biodegradation behavior, i.e., surface erosion reaction mechanism, to that of silicon nanomembranes, which can be described as nucleophilic attack model[40]. To further verify this surface erosion reaction mechanism, Raman scattering results are collected from germanium nanomembranes at different accelerated dissolution (10× PBS, 90 °C) periods, as shown in Supplementary Fig. 7. As the dissolution proceeds, the Raman scattering peak position of germanium nanomembrane has no obvious shift (constant as ~301 cm^{-1}) unless its complete dissolution (green curve), indicating that the lattice structure of the remaining germanium nanomembrane has no significant damage. HR-TEM images shown in Supplementary Fig. 6 also verify this surface erosion reaction mechanism. In terms of practical applications for bioelectronic implants, a recent study has demonstrated that various ions in tissue fluids will promote the nucleophilic attack on the exposed surface of biodegradable materials[41], which can further accelerate the degradation process. Moreover, the pH and temperature of the biofluidic can also strongly affect the dissolution rate of germanium[27]. Therefore, the obtained degradation rate (Fig. 2e) can only serve as guidance for the evaluation of the operation time of the biodegradable germanium electronics. Nevertheless, appropriate material strategies for the encapsulation layer can realize the control over the lifetime of biodegradable germanium electronics within the human body[42–44], and thus be suitable for the monitoring and/or treatment of either acute or chronic diseases[45,46].

Fabrication of biodegradable germanium-based sensors

The demonstrated biodegradability of germanium nanomembranes provides possibilities for the construction of biodegradable germanium electronics. In particular, the piezoresistance effect or the thermal effect on the electrical resistance of germanium forms the fundamentals for germanium-based strain or temperature sensors[47–49]. The following describes the fabrication process of germanium-based biodegradable sensors, as schematically illustrated in Fig. 3a. The top germanium nanomembrane of a GOI specimen is patterned into a serpentine ribbon via photolithography and inductively coupled plasma-reactive ion etching (ICP-RIE). The corresponding cross-section pseudo-colored SEM image is shown in Fig. 3b. Then, the buried oxide layer is partially etched by buffered hydrofluoric acid (BOE), forming a suspended germanium ribbon edge, as shown in Fig. 3c. After that, secondary photolithography is utilized to define the photoresist (PR) anchor underneath the germanium ribbon edge, as shown in Fig. 3d. Notably, the defined PR anchor can maintain the layout of the released germanium ribbons after the full removal of the buried oxide layer[50,51], as demonstrated in Fig. 3e, thus facilitating the deterministic assembly of germanium nanomembranes on desired substrates via the following transfer printing technique[52–54]. A cured PDMS slab is used as the stamp for the transfer and printing of the released germanium ribbons on the prepared biodegradable substrate, which consists of a multilayer configuration, i.e., iron foil as the substrate, PECVD SiO$_2$ as the electrical insulation layer, and SOG as the adhesion layer for enhancing the adhesive force between the printed germanium ribbons and the prepared substrate. Annealing treatment of the spin-coated SOG at nitrogen environment is performed to prompt the condensation reaction between Si(OH)$_4$ molecules to yield Si–O–Si bonds, which has been demonstrated to be biocompatible and biodegradable[55]. Finally, ultrathin Au electrodes are formed by electron beam evaporation, followed with a 200 nm SiO$_2$ encapsulation layer by PECVD. More details can be found in the Methods.

Characterizations on biodegradable germanium-based sensors

Figure 4a shows the change in the electrical resistance of a biodegradable germanium strain sensor varying with the applied strain, which is caused by bending the device (the inset of Fig. 4a), and the applied strain (ε) can be calculated by the following equation[56],

$$\varepsilon = \frac{t/2}{r} \times 100\%, \tag{1}$$

where r is the radius of curvature, t is the thickness of the device. Detailed calculation about the radius of curvature can be found in Supplementary Fig. 8. Furthermore, the GF, which represents an important parameter to evaluate the performance of a strain sensor, is expressed as[49],

$$GF = \frac{\Delta R/R_0}{\varepsilon}, \tag{2}$$

where ΔR is the change in resistance, R_0 is the initial resistance without bending. According to the experimental results and Eqs. (1) and (2), the GF of our fabricated device is estimated to be about 27, which is comparable to those of previously reported biodegradable strain sensors[57]. Notably, further improvement in GF of the demonstrated germanium-based device is available by optimizing its layout design, thickness, and the doping concentration of germanium nanomembranes[57].

The ability of a strain sensor to track the variation frequency of different human signals, such as the heartbeat (60–100 times per minute), respiration (12–20 times per minute), and Parkinson's disease (the tremor frequency mostly exhibits in 4–6 Hz)[58], is essential for the monitoring of human health status or for the recognition and assessment of human diseases. In this regard, the response of our fabricated biodegradable strain sensor to cycling bending signals with different bending frequencies is characterized. The bending frequency is controlled by a commercial force gauge (ESM303, Mark-10 Corporation). As shown in Fig. 4b, the fabricated sensor can response different bending operations with the frequencies of 0.45, 0.85, and 1.2 Hz, revealing the feasibility of sensing various human strain signals with a wide frequency range. Moreover, the response times of the sensor that responses to the
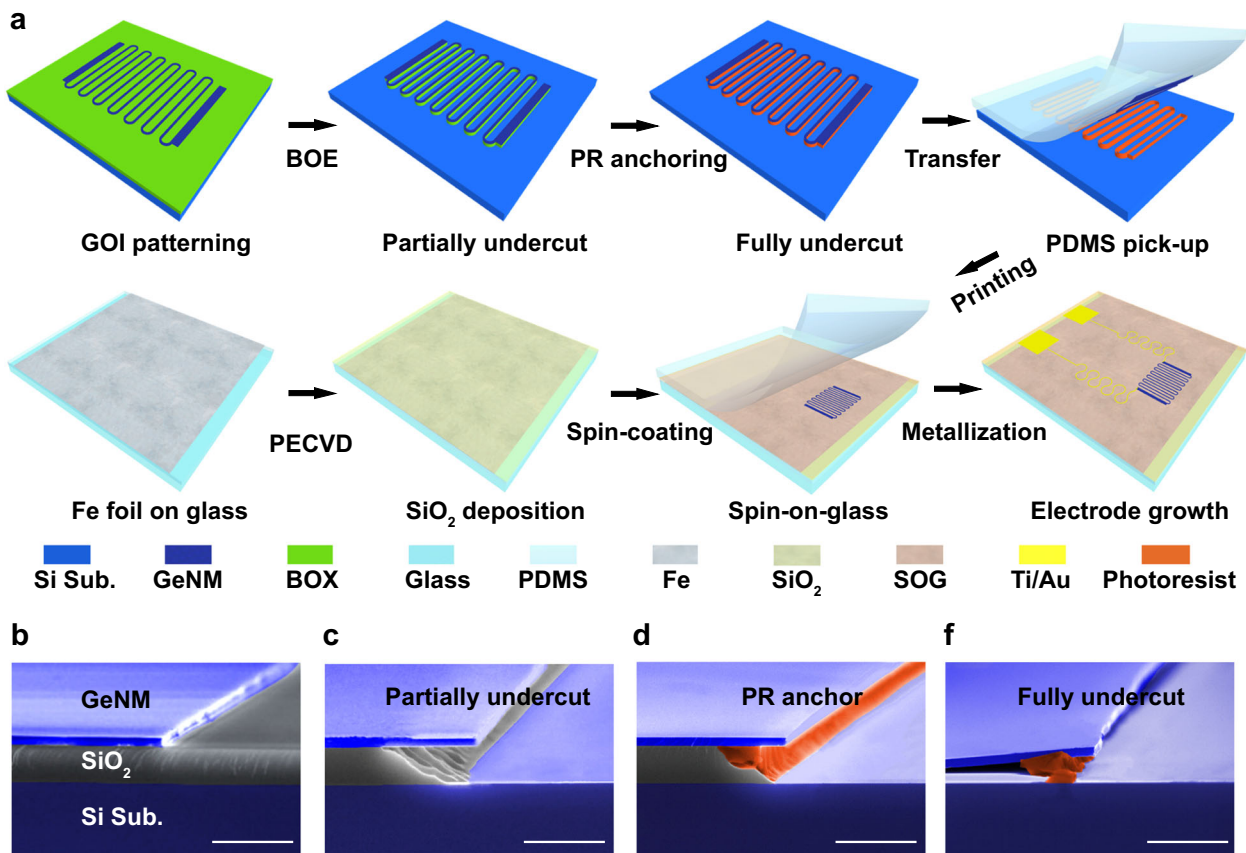
Fig. 3 Fabrication of the sensor. a Schematic illustration of key steps for the fabrication of biodegradable germanium nanomembrane-based sensors. **b–e** Pseudo-colored SEM images of a represented GOI at different fabrication steps, from left to right: photolithography and ICP-RIE define the germanium strip; partially undercutting the buried oxide layer realized by etching the buried oxide exposed and underneath the edge of strips in hydrofluoric acid; the formation of photoresist anchor; fully undercutting the buried oxide layer to release the defined germanium strips. Scale bar is 3 μm.

status from flatting to bending (t_{on}) and the status from bending to flatting (t_{off}) are 0.13 s and 0.12 s, respectively, as shown in Fig. 4c. Considering that the status switching between bending and flatting is realized by the movement of the slidable clamp, which is a gradual process for the utilized farce gauge, the actual response time of the sensor should be much smaller than the measured value. Characterizations at a cycling bending condition demonstrate the stability of the fabricated sensor. As shown in Fig. 4d, the sensor exhibits a consistent resistance change more than 600 bending cycles. Figure 4e and f shows the magnified results obtained at the initial and near the end of Fig. 4d, where no significant change in the stability is found.

Extended functionalities of this same platform are also available, such as the precision measurement of temperature, according to the temperature-dependent electrical resistance of germanium nanomembranes[48]. The resistance (or conductance) of germanium changes by an amount linearly proportional to temperature, as expressed by the following equation,

$$R = R_0(1 + \alpha(T - T_0)), \quad (3)$$

where R is the measured resistance at temperature T, R_0 is the initial resistance at temperature T_0 (i.e., room temperature), and α is the TCR. Figure 5a shows the in vitro setup for the measurement of the prepared biodegradable temperature sensor. A commercial temperature sensor is placed adjacent to the device for calibration, and a constant temperature incubator is used to preciously control the environmental temperature. Current–voltage (I–V) characteristics of the prepared sensor measured at different temperatures appear in Fig. 5b, exhibiting a good Ohmic contact between germanium

nanomembrane and gold electrode. Moreover, the resistance increases (see the inset of Fig. 5b) as the environment temperature gradually increases from 26.6 to 43.8 °C. Figure 5c summarizes the corresponding resistance varying with the temperature, revealing a good linear relationship (red fitting curve). According to Eq. (3), the TCR of the prepared biodegradable temperature sensor is calculated as 2.4×10^{-3}, which is comparable or much higher than those of previously reported biodegradable temperature sensors, as summarized in Table 1 of the Supporting Information. Notably, the TCR of a semiconductor-based temperature sensor can be further enhanced by the optimization in the dopant type and/or doping concentration[57], which is convenient for the utilized germanium nanomembranes.

Moreover, the prepared biodegradable temperature sensor exhibits an outstanding accuracy for temperature sensing, with a resolution of 0.1 °C, as shown in Supplementary Fig. 9 of the Supporting Information. Possible strategies, such as decreasing the doping concentration[59], modulating the Fermi energy level, and confining the carriers in intrinsic region via proper dopant impurities[60], optimized device configuration design[61], can further improve the temperature sensing resolution. Continuous temperature monitoring (20 minutes) of an incubator under different working modes, including turning off the electrical power for natural cooling-down process (I), opening the inner and outer doors for the accelerated cooling-down process (II), turning on the electrical power for the slow heating-up process (III), and closing the inner and outer doors for a constant temperature (IV), is performed by the prepared sensor, and a commercial temperature sensor is utilized for comparison. As shown in Fig. 5d, the prepared
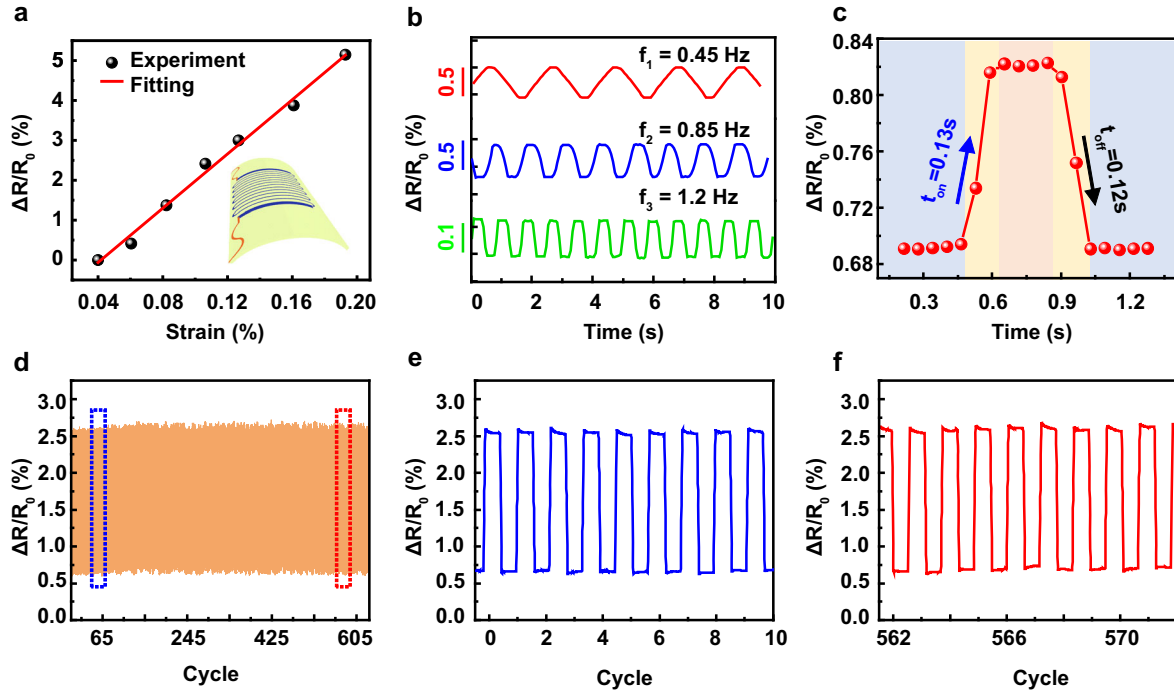
Fig. 4 Evaluations on the strain response of the fabricated sensor. a Experimental (black dots) and fitted (red line) changes in the resistance at different bending strains. **b** Real-time resistance variations of the sensor responding to cycling bending operations with different frequencies. **c** A magnified period of the resistance variation under cycling bending with the frequency of 1.2 Hz, and the response time to inflection and release of the bending strain is 0.13 s and 0.12 s, respectively. **d** Stability demonstration of the sensor responding to the cycling bending operation more than 600 cycles. **e, f** Magnified results of resistance variations obtained from the result displayed in **d** highlighted with dotted blue and red rectangles.

temperature sensor can exactly track the temperature variations of the incubator, revealing a high degree of agreement with the results obtained by the commercial sensor. These presented results suggest significant potentials of the developed biodegradable germanium nanomembrane-based temperature sensor for the real-time monitoring of physiological temperature with high accuracy and high sensing resolution.

The presence of both thermoresistive and piezoresistive effects within germanium nanomembranes offer possibilities for the fabrication of integrated biosensors, which can be utilized for the simultaneous monitoring of physiological signals, such as strain and temperature. Therefore, electrical properties of the prepared biodegradable germanium nanomembrane-based sensor under the co-exist of temperature and strain variations are characterized. Figure 6a shows the resistance mapping result of the device varies with both temperature and strain. It is clear that the measured resistance exhibits a linear relationship with the applied strain, with a temperature-independent slope, as revealed in Supplementary Fig. 10a of the Supporting Information. Similar results are also found in the linear relationship between the measured resistance and the environment temperature, with a strain-independent slope, as shown in Supplementary Fig. S10b of the Supporting Information. According to Eq. (2), the calculated average GF is 26.7 at different temperatures, as shown in Fig. 6b, with a small standard deviation of 0.7, suggesting the negligible temperature effect on the accuracy of strain sensing. Besides, the average temperature sensitivity at different applied strains is obtained as 105 Ω/°C, as shown in Fig. 6c, with a small standard deviation of 3.54 Ω/°C, indicating the negligible strain effect on the accuracy of temperature sensing.

These presented results of temperature-independent strain sensing and strain-independent temperature sensing offer

fundamentals for the integrated biosensing of strain and temperature. To verify the integrated biosensing capability, in vitro experiments are performed. As schematically illustrated in Fig. 6d, one side of the prepared sensor is attached to the outer wall of a circular beaker (I), where no strain is applied. After the full attachment (II), the strain will generate within the sensor due to the bending effect. Then, hot water is poured into the beaker (III), inducing an increased temperature applied to the sensor. After that, the reduction of temperature is realized by adding iced water into the beaker (IV). Finally, the sensor is released to its initial status (I). During the whole process, the sensor experiences complex crosstalk of different signals, successively including bending strain, increased temperature at the bending status, decreased temperature at the bending status, and released strain. Since the prepared biodegradable germanium nanomembrane-based sensor exhibits negligible temperature effect on strain sensing and negligible strain effect on temperature sensing, distinguishing the crosstalk between strain and temperature is expectable. Figure 6e shows the resistance variations (black curve) throughout the whole process illustrated in Fig. 6d. It is clear that the fabricated device can rapidly response to the change of the external environment conditions, which is also seen in Supplementary Video 1 of the Supporting Information. According to Eqs. (2) and (3), the co-effect of temperature and strain on the resistance of the prepared device can be described as[57],

$$R_{(\varepsilon,T)} = R_{(\varepsilon=0,T)}(1+G\varepsilon) = R_{(\varepsilon=0,\ T=T_0)}[1+\alpha(T-T_0)](1+G\varepsilon), \quad (4)$$

$R_{(\varepsilon,T)}$ is the final resistance affected by both strain and temperature, $R_{(\varepsilon=0,T)}$ is the resistance when only temperature is applied, G is the gauge factor, and $R_{(\varepsilon=0,T=T_0)}$ denotes the initial resistance without applied strain nor temperature variation (normally at room temperature). Based on Eq. 4, the strain and temperature at each operation status are calculated, as displayed
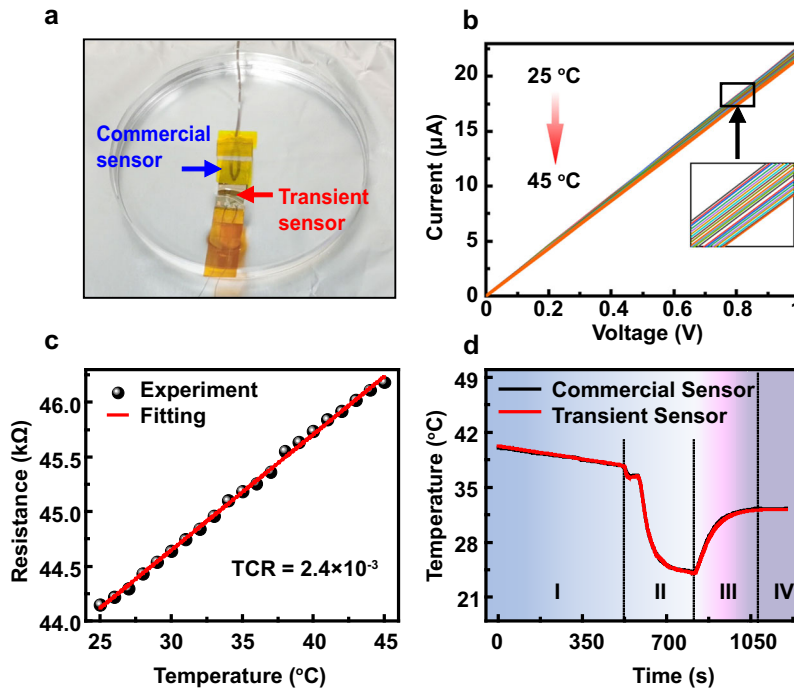
Fig. 5 Evaluations on the temperature response of the fabricated sensor. a In vitro setup for the measurement of biodegradable germanium nanomembrane-based sensor. A commercial temperature sensor is utilized for the calibration. **b** Current–voltage characteristics of the sensor at different temperatures. The inset is the magnified results highlighted with a black rectangle. **c** Experimental (symbol) and fitting (line) results of the changes in resistance of the sensor at different temperatures. **d** Comparison of the calibrated result obtained from the fabricated biodegradable germanium nanomembrane-based sensor (red curve) to that obtained from a commercial sensor (black curve).

Table 1. Comparison of key parameters measured from various biodegradable temperature/strain sensors fabricated with different materials.

Material	TCR	Sensitivity	Temp. range	Gauge factor	Ref.
Si	0.0012/°C	8 Ω/°C*	27–45 °C	20.9	7
Si	0.0005/°C	43 Ω/°C*	23–44 °C	30	57
Si	0.00611/°C	555 Ω/°C*	25–65 °C	–	58
Mg	0.00245/°C	70 Ω/°C	20–50 °C	–	62
Mg	0.08/°C	0.014 Ω/°C	34–52 °C	–	63
Ge	**0.0024/°C**	**105 Ω/°C**	**25–45 °C**	**27**	**This work**

*Represents the data calculated from the reference.
Bold values represent our work.

in Fig. 6e. Notably, the obtained strain and temperature are consistent with the theoretical strain value (calculated by Eq. (1)) and the measured temperature value by a commercial sensor, respectively.

In summary, the results presented here provide the basis for germanium electronics to serve as biodegradable and implantable platforms, with promising applications in biomedical engineering. The gas-free degradation process and ability to distinguish the crosstalk of different physiological signals, in particular the real-time monitoring of strain and temperature variations, in platforms that are built entirely with biocompatible and bioresorbable materials represent the main points of interest. Systematic studies reveal the temperature-independent strain sensing and strain-independent temperature sensing of the proposed biodegradable germanium nanomembrane-based sensors. The presented in vitro demonstrates foreshadow opportunities in the integrated biosensing of physiological signals, as potential highly dense platforms for the accuracy diagnose of human health status.

METHODS

Fabrication of biodegradable germanium sensors

Fabrication began with the commercially available GOI wafer, with the top germanium nanomembrane being 200 nm in thick and the buried oxide layer being 2 μm in thick. Photolithography and inductively coupled plasma-reactive ion etching (ICP-RIE) were utilized to define the top germanium nanomembrane into serpentine strip with a width of 20 μm. Then, the patterned GOI was immersed in HF (49%, Macklin) for 2 min to partly etch the buried oxide. The following spin-coating of photoresist enabled the full cover of the patterned germanium nanomembrane, as well as the fill of photoresist into the beneath of the suspended germanium strip. Then, another photolithography with full-exposure of ultra-violet light was used to define the anchor structure underneath the suspended strip. After that, the prepared sample was immersed in HF for 30 min to fully remove the buried oxide layer, thus releasing the patterned serpentine strip, which was picked up and transferred to the prepared biodegradable substrate by a PDMS stamp. Finally, Ti/Au (5/30 nm) electrodes grown by electron beam evaporation and SiO₂ encapsulation layer (200 nm) deposited by PECVD completed the fabrication of a biodegradable germanium sensor.

Preparation of biodegradable substrates

A spin-coated PDMS (10:1) on glass served as the temporary support for the biodegradable substrates. Biodegradable metal foils, such as Fe (30 μm in thickness) and Mo (50 μm in thickness), were attached to the partly cured PDMS/glass substrate. After the fully curing treatment (70 °C, 3 h), an electrical insulation layer of SiO₂ (200 nm) was grown by PECVD. Then, a SOG layer was spin-coated (800 rpm, 30 s) to serve as the adhesion layer for the subsequent transfer printing of germanium nanomembranes. After the transfer printing, annealing treatment that can prompt the condensation reaction between Si(OH)₄ molecules to yield Si–O-Si bonds was performed in a nitrogen ambient at 270 °C for 1 h.
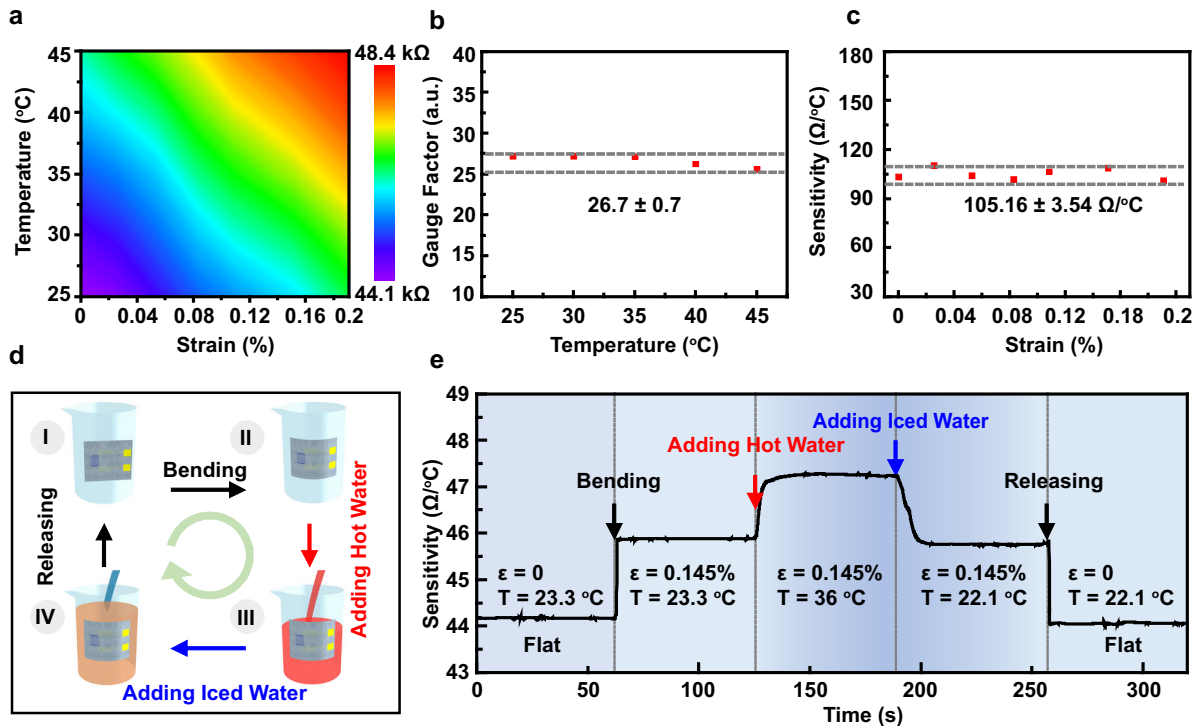
Fig. 6 Evaluations on the integrated response to strain and temperature. a Mapping result of the resistance measured from the sensor under different strains and temperatures. **b** Gauge factor variations of the sensor at different temperatures. **c** Sensitivity variations of the sensor for sensing temperature at different applied strains. **d** Schematic diagram of the in vitro experiment to evaluate the ability of the sensor for the integrated biosensing of strain and temperature. **e** Resistance variations obtained from the sensor that responses to different strain and temperature conditions in (**d**).

Dissolution of germanium and characterizations

The dissolution of germanium started with the patterning of a GOI wafer. The thickness of top germanium nanomembrane was 50 nm. Photolithography and ICP-RIE were utilized to define the germanium relief array, with the dimension of a single relief of $30 \times 30\,\mu m$ and a spacing of $30\,\mu m$. Then, the dissolution of the germanium relief array was accomplished by soaking in PDMS well-contained DI water or PBS at the physiological temperature, i.e., 37 °C, which was controlled by a constant temperature incubator. After the dissolution at different times, the sample was immediately rinsed with DI water, and dried by a condensed nitrogen gas gun. Then, AFM, SEM, and Raman scattering measurements were performed to monitor the corresponding height reduction and crystalline quality of germanium reliefs, which were degraded at different times.

Test of the sensor

The electrical properties of the sensor were measured by using a digital multimeter (Keysight 2450). The evaluation of the strain response was performed by measurements of the electrical resistance of the sensor, which was attached to circular subjects with different curvature radiuses. The strain response to the cycling bending strain, which was realized by a commercial force gauge (ESM303, Mark-10 Corporation), was evaluated by the measurement of the electrical resistance. The evaluation of the temperature response was performed by measurements of the electrical resistance of the sensor under different environment temperatures, which were controlled by a constant temperature incubator, and a commercial temperature sensor was utilized for the calibration.

DATA AVAILABILITY

The data generated and analyzed during the study are available from the corresponding authors on a reasonable request.

REFERENCES

1. Hwang, S. W. et al. A physically transient form of silicon electronics. *Science* **337**, 1640–1644 (2012).
2. Wu, X. & Guo, Q. Bioresorbable photonics: materials, devices and applications. *Photonics* **8**, 235 (2021).
3. Wei, Z., Xue, Z. & Guo, Q. Recent progress on bioresorbable passive electronic devices and systems. *Micromachines* **12**, 600 (2021).
4. Shin, J. et al. Bioresorbable optical sensor systems for monitoring of intracranial pressure and temperature. *Sci. Adv.* **5**, eaaw1899 (2019).
5. Liu, K., Tran, H., Feig, V. R. & Bao, Z. Biodegradable and stretchable polymeric materials for transient electronic devices. *MRS Bull.* **45**, 96–102 (2020).
6. Koo, J. et al. Wireless bioresorbable electronic system enables sustained non-pharmacological neuroregenerative therapy. *Nat. Med.* **24**, 1830–1836 (2018).
7. Shin, J. et al. Bioresorbable pressure sensors protected with thermally grown silicon dioxide for the monitoring of chronic diseases and healing processes. *Nat. Biomed. Eng.* **3**, 37–46 (2019).
8. Lu, L. et al. Biodegradable monocrystalline silicon photovoltaic microcells as power supplies for transient biomedical implants. *Adv. Energy Mater.* **8**, 1703035 (2018).
9. Guo, Q. et al. A bioresorbable magnetically coupled system for low-frequency wireless power transfer. *Adv. Funct. Mater.* **29**, 1905451 (2019).
10. Hwang, S. W. et al. 25th anniversary article: materials for high-performance biodegradable semiconductor devices. *Adv. Mater.* **26**, 1992–2000 (2014).
11. Boutry, C. M. et al. Biodegradable and flexible arterial-pulse sensor for the wireless monitoring of blood flow. *Nat. Biomed. Eng.* **3**, 47–57 (2019).
12. You, C., Zhao, H., Guo, Q. & Mei, Y. Material strategies for on-demand smart transient electronics. *MRS Bull.* **45**, 129–134 (2020).
13. Hwang, S. W. et al. Biodegradable elastomers and silicon nanomembranes/nanoribbons for stretchable, transient electronics, and biosensors. *Nano Lett.* **15**, 2801–2808 (2015).
14. Boutry, C. M. et al. A stretchable and biodegradable strain and pressure sensor for orthopaedic application. *Nat. Electron.* **1**, 314–321 (2018).
15. Yin, L. et al. Materials, designs, and operational characteristics for fully biodegradable primary batteries. *Adv. Mater.* **26**, 3879–3884 (2014).
16. Bai, W. et al. Bioresorbable photonic devices for the spectroscopic characterization of physiological status and neural activity. *Nat. Biomed. Eng.* **3**, 644–654 (2019).

17. Yu, K. J. et al. Bioresorbable silicon electronics for transient spatiotemporal mapping of electrical activity from the cerebral cortex. *Nat. Mater.* **15**, 782–791 (2016).

18. La Mattina, A. A., Mariani, S. & Barillaro, G. Bioresorbable materials on the rise: from electronic components and physical sensors to in vivo monitoring systems. *Adv. Sci.* **7**, 1902872 (2020).

19. Chang, J.-K. et al. Biodegradable electronic systems in 3D, heterogeneously integrated formats. *Adv. Mater.* **30**, 1704955 (2018).

20. Yun, Y. et al. Revolutionizing biodegradable metals. *Mater. Today* **12**, 22–32 (2009).

21. Zberg, B., Uggowitzer, P. J. & Loffler, J. F. MgZnCa glasses without clinically observable hydrogen evolution for biodegradable implants. *Nat. Mater.* **8**, 887–891 (2009).

22. Song, G. & Song, S. A possible biodegradable magnesium implant material. *Adv. Eng. Mater.* **9**, 298–302 (2007).

23. Dagdeviren, C. et al. Transient, biocompatible electronics and energy harvesters based on ZnO. *Small* **9**, 3398–3404 (2013).

24. Jin, S. H. et al. Water-soluble thin film transistors and circuits based on amorphous indium-gallium-zinc oxide. *ACS Appl. Mater. Interfaces* **7**, 8268–8274 (2015).

25. Chiong, J. A. et al. Integrating emerging polymer chemistries for the advancement of recyclable, biodegradable, and biocompatible electronics. *Adv. Sci.* **8**, 2101233 (2021).

26. Hwang, S. W. et al. Dissolution chemistry and biocompatibility of single-crystalline silicon nanomembranes and associated materials for transient electronics. *ACS Nano* **8**, 5843–5851 (2014).

27. Kang, S. K. et al. Dissolution chemistry and biocompatibility of silicon- and germanium-based semiconductors for transient electronics. *ACS Appl. Mater. Interfaces* **7**, 9297–9305 (2015).

28. Wang, Q. et al. Germanium nanowire field-effect transistor with SiO_2 and High-κ HfO_2 gate dielectrics. *Appl. Phys. Lett.* **83**, 2432–2434 (2003).

29. Rogers, J. A., Lagally, M. G. & Nuzzo, R. G. Synthesis, assembly and applications of semiconductor nanomembranes. *Nature* **477**, 45–53 (2011).

30. Guo, Q., Di, Z., Lagally, M. G. & Mei, Y. Strain engineering and mechanical assembly of silicon/germanium nanomembranes. *Mater. Sci. Eng. R. Rep.* **128**, 1–31 (2018).

31. Carlander, U. et al. Macrophage-assisted dissolution of gold nanoparticles. *ACS Appl. Bio Mater.* **2**, 1006–1016 (2019).

32. Balfourier, A. et al. Unexpected intracellular biodegradation and recrystallization of gold nanoparticles. *Proc. Natl Acad. Sci. USA* **117**, 103–113 (2020).

33. Danscher, G. In vivo liberation of gold ions from gold implants: autometallographic tracing of gold in cells adjacent to metallic gold. *Histochem. Cell Biol.* **117**, 447–452 (2002).

34. Zainali, K. et al. Particulate gold as an anti-inflammatory mediator in bone allograft-an animal study. *J. Biomed. Mater. Res A* **95**, 956–963 (2010).

35. Zainali, K. et al. Assessment of modified gold surfaced titanium implants on skeletal fixation. *J. Biomed. Mater. Res Part A* **101**, 195–202 (2013).

36. McCarrick, S. et al. Gold nanoparticles dissolve extracellularly in the presence of human macrophages. *Int. J. Nanomed.* **16**, 5895–5908 (2021).

37. Li, R. et al. A flexible and physically transient electrochemical sensor for real-time wireless nitric oxide monitoring. *Nat. Commun.* **11**, 3207 (2020).

38. Pillarisetty, R. Academic and industry research progress in germanium nanodevices. *Nature* **479**, 324–328 (2011).

39. Harvey, W. W. & Gatos, H. C. The reaction of germanium with aqueous solution. *J. Electrochem. Soc.* **105**, 654–660 (1958).

40. Wang, L. et al. Geometrical and chemical-dependent hydrolysis mechanisms of silicon nanomembranes for biodegradable electronics. *ACS Appl. Mater. Interfaces* **11**, 18013–18023 (2019).

41. Yin, L. et al. Mechanisms for hydrolysis of silicon nanomembranes as used in bioresorbable electronics. *Adv. Mater.* **27**, 1857–1864 (2015).

42. Li, J. et al. Ultrathin, high capacitance capping layers for silicon electronics with conductive interconnects in flexible, long-lived bioimplants. *Adv. Mater. Technol.* **5**, 1900800 (2019).

43. Song, E. et al. Ultrathin trilayer assemblies as long-lived barriers against water and ion penetration in flexible bioelectronic systems. *ACS Nano* **12**, 10317–10326 (2018).

44. Lee, Y. K. et al. Kinetics and chemistry of hydrolysis of ultrathin, thermally grown layers of silicon oxide as biofluid barriers in flexible electronic systems. *ACS Appl. Mater. Interfaces* **9**, 42633–42638 (2017).

45. Chiang, C. et al. Development of a neural interface for high-definition, long-term recording in rodents and nonhuman primates. *Sci. Transl. Med.* **12**, eaay4682 (2020).

46. Phan, H. P. et al. Long-lived, transferred crystalline silicon carbide nanomembranes for implantable flexible electronics. *ACS Nano* **13**, 11572–11581 (2019).

47. Smith, C. S. Piezoresistance effect in germanium and silicon. *Phys. Rev.* **94**, 42–49 (1954).

48. Morin, F. J., Geballe, T. H. & Herring, C. Temperature dependence of the piezoresistance of high-purity silicon and germanium. *Phys. Rev.* **105**, 525–539 (1957).

49. Barlian, A. A. et al. Review: semiconductor piezoresistance for microsystems. *Proc. IEEE* **97**, 513–552 (2009).

50. Yang, Y. et al. Arrays of silicon micro/nanostructures formed in suspended configurations for deterministic assembly using flat and roller-type stamps. *Small* **7**, 484–491 (2011).

51. Bai, W. et al. Flexible transient optical waveguides and surface-wave biosensors constructed from monocrystalline silicon. *Adv. Mater.* **30**, 1801584 (2018).

52. Carlson, A. et al. Transfer printing techniques for materials assembly and micro/nanodevice fabrication. *Adv. Mater.* **24**, 5284–5318 (2012).

53. Meitl, M. A. et al. Transfer printing by kinetic control of adhesion to an elastomeric stamp. *Nat. Mater.* **5**, 33–38 (2005).

54. Guo, Q. et al. Deterministic assembly of flexible Si/Ge nanoribbons via edge-cutting transfer and printing for van der Waals heterojunctions. *Small* **11**, 4140–4148 (2015).

55. Kang, S.-K. et al. Biodegradable thin metal foils and spin-on glass materials for transient electronics. *Adv. Funct. Mater.* **25**, 1789–1797 (2015).

56. Mao, L., Meng, Q., Ahmad, A. & Wei, Z. Mechanical analyses and structural design requirements for flexible energy storage devices. *Adv. Energy Mater.* **7**, 1700535 (2017).

57. Kang, S. K. et al. Bioresorbable silicon electronic sensors for the brain. *Nature* **530**, 71–76 (2016).

58. Ko, G. J. et al. Biodegradable, flexible silicon nanomembrane-based NOx gas sensor system with record-high performance for transient environmental monitors and medical implants. *NPG Asia Mater.* **12**, 71 (2020).

59. Sang, M. W. et al. Piezoresistive strain sensors and multiplexed arrays using assemblies of single-crystalline silicon nanoribbons on plastic substrates. *IEEE Trans. Electron Devices* **58**, 4074–4078 (2011).

60. Sang, M. et al. Ultrahigh sensitive Au-doped silicon nanomembrane based wearable sensor arrays for continuous skin temperature monitoring with high precision. *Adv. Mater.* **34**, 2105865 (2022).

61. Childs, P. R. N., Greenwood, J. R. & Long, C. A. Review of temperature measurement. *Rev. Sci. Instrum.* **71**, 2959–2978 (2000).

62. Salvatore, G. A. et al. Biodegradable and highly deformable temperature sensors for the internet of things. *Adv. Funct. Mater.* **27**, 1702390 (2017).

63. Son, D. et al. Bioresorbable electronic stent integrated with therapeutic nanoparticles for endovascular diseases. *ACS Nano* **9**, 5937–5946 (2015).

ACKNOWLEDGEMENTS

AUTHOR CONTRIBUTIONS

Q.L. Guo, Y.F. Mei, and Z.F. Di designed and supervised the research; H.N. Zhao led the fabrication and characterization with assistance from Z.Y. Xue, X.Z. Wu, Z.H. Wei, Q.Y. Guo, M. Xu, C.Y. Qu, C.Y. You, and M. Zhang; H.N. Zhao, Y.F. Mei, Z.F. Di, and Q.L. Guo wrote the text and designed the figures. All authors commented on the paper.

COMPETING INTERESTS

The authors declare no competing interests.

ADDITIONAL INFORMATION

Supplementary information The online version contains supplementary material available at https://doi.org/10.1038/s41528-022-00196-2.

Correspondence and requests for materials should be addressed to Yongfeng Mei, Zengfeng Di or Qinglei Guo.

Reprints and permission information is available at http://www.nature.com/reprints

Publisher's note Springer Nature remains neutral with regard to jurisdictional claims in published maps and institutional affiliations.